Author’s response to Review RC1 by Emmanuel Dekemper

We are very gratefully acknowledging the comments of Emmanuel Dekemper. The comments are highly helpful in both, in enhancing the clarity of the presented technique and model.

For clarity we answer the specific comments directly (bold printed). The reviewer comments are set in italic font, the authors’ responses in normal font. We added a new Figure (Fig. 2) and included a SO2 flux calculation at the end of Section 3.3 and in Section 4. In several places throughout the manuscript we modified and extended sentences yielding minor changes to the manuscript.

1.1 The abstract

Reviewer’s comment: Although the abstract is a good summary of the manuscript (high level description of the instrument concept, and the experimental results achieved), I think it is slightly ex-aggerating the demonstrated capabilities of the instrument. For instance, it is claimed that the instrument does the job for SO2, BrO, and NO2, whereas only the first species is addressed. I understand that the prototype was designed to correlate with the SO2 structures, but therefore, at least a theoretical simulation of performance for the other species should have been presented. In absence of this, the BrO and NO2 capabilities should only be referred to as potential future applications. The same goes for the statement that the instrument allows to determine gas fluxes, while this aspect is also not discussed in the paper. The factual performance of the prototype is also a bit misleading: the claimed integration time of 1s is, as far as I could understand, the integration time of a single image, not yet the temporal resolution of the geophysical product (presumably closer to 5 seconds) as it seems currently suggested. Hence, I would recommend to rework a bit the abstract such that undemonstrated, though potentially achievable goals are not presented as conclusions of the work.

Author’s response:

- Indeed, we did only present imaging measurement results of volcanic SO_2 emissions. Of course, the FPI employed for that was specifically designed to correlate with SO_2. However, the camera prototype itself was not solely implemented for SO_2. Replacing the BPF and the FPI, by one that is designed for BrO or NO_2 the camera can be used for measuring further gas species. Within this manuscript we did in fact not present theoretical simulation of the performance for gases other than SO_2 since these were already presented in a former manuscript (Kuhn et al. 2019). We will therefore change the claim to be able to measure BrO and NO2 to future applications.

  We changed the sentence (submitted manuscript lines: 4 - 6):
  “Matching the FPIs distinct, periodic transmission features to the characteristic differential absorption structures of the investigated trace gas allows to measure differential atmospheric column density (CD) distributions of numerous trace gases, e.g. sulphur dioxide (SO_2), bromine monoxide (BrO), or nitrogen dioxide (NO_2), with high spatial and temporal resolution.”

To (revised manuscript lines: 3 - 6):
“Matching the FPIs distinct, periodic transmission features to the characteristic differential absorption structures of the investigated trace gas allows to measure differential atmospheric column density (CD) distributions of numerous trace gases with high spatial and temporal resolution. Here we demonstrate measurements of sulphur dioxide (SO_2) while earlier model calculations show that bromine monoxide (BrO) and nitrogen dioxide (NO_2) are also possible.”

- Further, we stated that we can determine gas fluxes since it is usually possible to retrieve fluxes from an image time series with sufficient high spatial resolution. However, the viewing geometry on the day of measurement was quite unfavourable as the plume propagation direction and field of view direction only had low inclination of 19° in contrast to ideal condition with a plume perpendicular to the viewing direction. Also, the fact that the plume was partly covered by the crater flank only allows to calculate a lower limit to the actual gas flux. Nonetheless, we now include a flux calculation in the article and discussing the unfavourable conditions for this particular example, which lead to a rather high measurement error but is showing the capability of IFPICS to determine fluxes.

We added the sentences (revised manuscript lines: 238 - 259):
“After the proof of concept, showing the capability of IFPICS to determine SO_2 CD images it is possible to determine fluxes from a CD image time series. Especially, if the series allows to trace back individual features in consecutively recorded images it can be used to directly determine the plume velocity using the approach of cross-correlation (e.g. McGonigle et al., 2005; Mori and Burton, 2006; Dekemper et al., 2016) or optical flow algorithms (e.g. Kern et al., 2015b) and to determine the plume propagation direction (e.g. Klein et al., 2017). However, the viewing geometry on the day of our measurement was unfavourable as it was not possible to reach another measurement location due to a lack in infrastructure. The plume propagation direction and central line of sight show an inclination of 19° only, resulting in high pixel contortions, especially for pixel close to the edges of the FOV. Further, significant parts of the plume are covered by the crater flank due to its propagation direction. For the sake of completeness, we would like to give a rough estimate on the SO_2 flux obtained from our data.
The SO_2 flux Φ_{SO2} is determined by integrating the SO_2 CD along a transect through the volcanic plume and subsequent multiplication by the wind velocity perpendicular to the FOV direction, however due to the viewing geometry issues we will use external wind data (direction: 5°; velocity $v_{wind} \approx 6$ m s^{-1} (data from UWYO)) for the calculation. As the camera pixel size is finite the integral is replaced by a discrete summation over the pixel n

$$\Phi_{SO2} = v_{\perp} \sum_n S_{SO2;n} \cdot h_n$$

including the perpendicular wind velocity $v_{\perp}$, the SO2 CD $S_{SO2;n}$ and the pixel extent h_n. The perpendicular wind velocity can directly be calculated from geometric considerations (see Fig. 5, (a)), accounting to $v_{\perp} \approx \sin(19°)\, v_{wind} \approx 2$ m s^{-1}. To determine the pixel extent the distance between the volcanic plume and the location of measurement is required. In the centre of the FOV this distance is ≈3500m yielding h_n ≈2,7 m. To keep the impact of pixel contortions low the plume transect is located centrally in the FOV at column 250 and ranging from rows n = 230 to 330. Using these quantities, we retrieve a mean SO_2 mass flux for the measurement of $\Phi_{SO2} = (84\pm11)\ t\ d^{-1}$ for the investigated plume of the South East crater. Nevertheless, the flux should be regarded as lower limit, since the plume was covered by crater flank to an unknown extent."

We changed & relocated the sentence (submitted manuscript lines: 231 - 233): "Also, the imaging technique lends itself to the determination of gas fluxes. For instance, the wind velocity and also the angle between the observation direction and plume propagation direction can be determined from the image series."

To (revised manuscript lines: 266 - 271):
"Also, the imaging technique lends itself to the determination of gas fluxes and we obtained an SO2 mass flux of $\Phi_{SO2} = (84\pm11)\ t\ d^{-1}$ for Mt. Etna's South East crater plume. However, due to unfavourable conditions in the viewing geometry the retrieved flux should be treated as a lower limit. In general, it is possible to apply optical flow algorithms on image series acquired under more ideal viewing geometry conditions (e.g. Kern et al., 2015b). These allow to determine the plume velocity and angle between the observation direction and plume propagation direction in order to retrieve accurate so2 fluxes (e.g. Klein et al., 2017)."

- We added the total time required for the acquisition of a pair of images, including tilting, and saving the images, which was 5.5 seconds for the used prototype setup. In further instrument versions, image readout and motor movement are negligible compared to the exposure time of 1 s.

  We further changed the sentence (submitted manuscript lines: 9 - 11):
  "In a field campaign, we recorded the temporal CD evolution of SO2 in the volcanic plume of Mt. Etna with an integration time of 1 s and 400x400 pixels spatial resolution. The first IFPICS prototype can reach a detection limit of $2{,}1\times10^{17}$ molec $cm^{-2}\ s^{-1}$, which is comparable to traditional and much less selective volcanic SO_2 imaging techniques."

  To (revised manuscript lines: 9 - 14):
  "In a field campaign, we recorded the temporal CD evolution of SO_2 in the volcanic plume of Mt. Etna with an exposure time of 1 s per image and 400 x 400 pixel spatial resolution. The temporal resolution of the time series was limited by the available non-ideal prototype hardware to about 5.5 s. Nevertheless, a detection limit of $2{,}1\times10^{17}$ molec cm^{-2} could be reached, which is comparable to traditional and much less selective volcanic SO2 imaging techniques."

1.2 The instrumental model

<u>Reviewer's comment:</u> The mathematics describing the measurements have been carefully developed, and the reader will appreciate the author's will to integrate all the meaningful aspects of the model (in particular the splitting of the instrument transfer function into different multiplicative terms). However, I have two remarks regarding this section:

1. *Less experienced readers might be lost in this section because it lacks a drawing representing the light paths involved. Supporting the mathematical description with a figure showing that eq.(2) refers to the light path originating from the Sun and going up to the point of scattering into the instrument line of sight would already be helpful. Having two rays illustrating the difference between Ii, and I0,i would also be appreciated.*

2. *Recalling the reader about the fundamental FPI equation is valuable. However, eq.(7) appears to be a step too far, especially that the weighting function term N remains mysterious at the end. I believe that the discussion on the effective transmission spectrum of the FPI is an important point. But because the reader will anyway not be able to reproduce your model (because of the undetermined term N), it is better to illustrate the effect of increasing the acceptance angle (or the tilt angle) on the FPI transmission with the help of a figure (a bit like fig.(1),but emphasizing the change of T_{FPI} as a function of these angles). Also, I found it not so clearly explained that the way the comb of the FPI is shifted (to go from setting A to B and back) is by rotating the FPI axis. A few words about the different means of performing this shift with nowadays FPI technologies (e.g. MEMS, piezo), and the trade off which led to the selection of the tilting approach would be appreciated.*

<u>Author's response:</u>

Point 1: This is a good suggestion. We extended the introduction of the mathematical model by a graphical representation, which is now Fig. 2.

> "A 2D UV-sensitive CMOS sensor (SCM2020-UV provided by *EHD imaging*) is used to acquire images."

We included a new figure; Fig. 2:

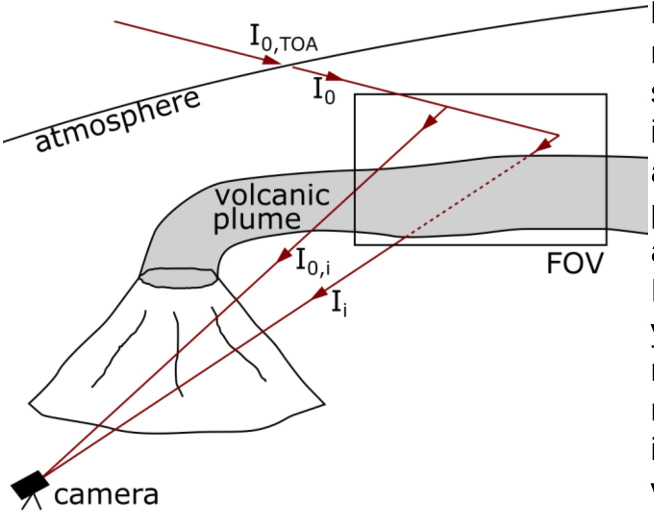

Figure 2. Schematic of the IFPICS measurement geometry including the simulated radiances used in the instrument model. The incident top of atmosphere (TOA) radiation $I_{0,TOA}$ is propagating through the atmosphere and is potentially scattered into the IFPICS camera field of view (FOV) yielding the scattered skylight radiance I_0. The camera records radiation in the respective FPI settings i = A and B that either traverses the volcanic plume I_i or originates from a plume free area within the FOV $I_{0,i}$.

Point 2: We had many thoughts about how detailed we should present our applied model. We tried to make it as detailed as possible and the representation of the final equation (Eq. (7)) was frequently discussed among the authors. Due to its high complexity, requiring three case analyses, all resulting in a different function, we ultimately only showed a more general equation trying to emphasize the basic principle. The quantity N representing the weighting and is given by the integral in Eq. 7 excluding the integrand $T_{FPI,i}$. We will include a description in the revised version of the manuscript.
Thanks for the comment concerning the shift of the FPI comb. We will emphasize this point in both, the introduction of the model, and in the description of the prototype setup. Further we will add a description to the manuscript why we use a tilting approach.

We added the sentences (revised manuscript lines: 104 - 107):
"The FPI used in this work is static and air-spaced, meaning d, n, and R are fixed. Hence, the incidence angle α_i is the exclusive free parameter available to tune the FPIs transmission spectrum $T_{FPI;i}$ between settings i = A and i = B respectively. The change in α_i is achieved by tilting the FPI optical axis with respect to the imaging optical axis (see Section 2.2)."

We changed the sentence (submitted manuscript lines: 107 - 108):
"Thereby, $N(\gamma(\alpha_i,\omega_c))$ denotes the weighting function, ϑ the polar angle and φ the azimuth angle of the spherical integration within boundaries defined by the tilted cone shaped light beams."

To (revised manuscript lines: 115 - 117):
"Thereby, $N(\gamma(\alpha_i,\omega_c))$ denotes the weighting function with $N(\gamma(\alpha_i,\omega_c))= \iint \sin\vartheta \, d\vartheta \, d\varphi$ given by the integral in Eq. 7 excluding the integrand $T_{FPI,I}$ itself, ϑ the polar angle and φ the azimuth angle of the spherical integration within boundaries defined by the tilted cone shaped light beams."

We changed and extended the sentence (submitted manuscript lines: 125 - 127):
The static air-spaced FPI (d, n and R fixed, provided by *SLS Optics Ltd*.) can be tilted within the parallelised light path in order to tune its spectral transmission T^{eff}_{FPI} between setting A and B via variation of the incidence angle α (see Section 2.1).

To (revised manuscript lines: 135 - 138):
The FPI is the central optical element of the IFPICS prototype and is implemented as static air-spaced etalon with fixed d, n, and R (provided by *SLS Optics Ltd*.). The mirrors are separated using ultra low expansion glass spacers to maintain a constant mirror separation d and parallelism over the large clear aperture of 20 mm even under highly variable environmental conditions. In order to tune the spectral transmission T^{eff}_{FPI} between setting A and B a variation of the incidence angle α is applied.

We added the sentence (revised manuscript lines: 141 - 143):
We favour the approach of tilting the FPI over changing internal physical properties like, e.g. the mirror separation d by piezoelectric actuators, as it keeps simplicity, robustness, and accuracy high for measurements under non-laboratory conditions.

1.3 Minor comments

- *<u>Reviewer's comment</u>: p.2,l.26: The NO2 camera, presented in Dekemper et al. 2016, has a spectral resolution of 0.6nm at 440nm... The statement that native spectral imagers have a "strongly reduced spectral resolution" is therefore not correct. It is not because the classical filter-based SO2 cameras have a poor spectral resolution that all other spectral imagers have the same drawback, especially when the filter technology is completely different.*

  <u>Author's response:</u>

  We changed and extended the sentence (submitted manuscript lines: 24 - 30):
  "A third approach applies a small number of (typically two) wavelength channels by using wavelength selective optical elements for the entire image frame, thereby usually strongly reducing the spectral resolution (e.g. Mori and Burton, 2006; Dekemper et al., 2016). The high spectral resolution of the first two, spectrograph based approaches allows the accurate and simultaneous identification of several trace gases, however, the light throughput and the scanning process severely limit the temporal resolution. The third approach can be quite fast, the trace gas selectivity, however, strongly depends on the correlation of trace gas absorption with the wavelength selective elements and usually is rather marginal."

  To (revised manuscript lines: 26 - 34):
  "The high spectral resolution of the spectrograph based techniques allows the accurate and simultaneous identification of several trace gases, however, the light throughput and the scanning process severely limit the temporal resolution. A third approach applies tunable filters to resolve the trace gas spectral features, e.g. acousto-optical tunable filter (Dekemper et al., 2016), as wavelength selective elements for an entire image frame. The application of tunable filters can have high spectral resolution and hence high trace gas selectivity, however, due to limited light throughput the temporal resolution lies in the order of minutes. A fourth imaging technique uses a small number (typically two) wavelength channels selected by static filters, e.g. interference filters (Mori and Burton, 2006). This approach can be quite fast with a temporal resolution in the order of seconds, the trace gas selectivity, however, strongly depends on the correlation of trace gas absorption with the wavelength selective elements and usually is rather marginal."

- *<u>Reviewer's comment:</u> I was wondering if the tilting of the FPI in order to go from setting A to B was introducing a shift of the respective images onto the detector? Is there a re-alignment step needed in the pre-processing of the data? If yes, then this is worth a couple of sentences addressing this aspect.*

  <u>Author's response</u>: Yes, indeed the tilting is inducing a linear shift of the respective images A and B on the detector. Therefore, a realignment step for the processing is performed accounting for a shift of 6 pixels. In the revised version we will address this point in Section 2.2 and 3.1.

We added the sentence (revised manuscript lines: 143 - 145):
"However it need to be considered, that the tilting of the FPI will generate a linear shift between the respective images acquired in setting A and B, requiring an alignment in the evaluation process."

We added the sentence (revised manuscript lines: 166 - 167):
"The tilt of the FPI generates a linear shift between the recorded on-band and off-band images on the detector and accounts for 6 pixel using tilt angles α_i. This shift needs to be corrected before cross evaluating images recorded in setting A and B."

- *Reviewer's comment: Section 3.2: Your forward model uses a geometric air mass factor to estimate the SCD of O3. The model was validated for a relatively small SZA with the two gas cells. However, your field measurements were performed with a much larger SZA of almost 80°. Don't you expect a bias coming from the geometric AMF in that circumstances?*

  Author's response: Yes indeed, large SZA can impact the calibration function retrieved by the instrument model. We geometrically recalculated the O_3 AMF assuming a homogeneous spherical shell of O_3 within a spherical nonrefracting atmosphere. For an SZA of 78° the retrieved change in the O_3 AMF is -7.5% translating to a sensitivity increase of +3.6% of the calculated calibration function. As the bias is rather small, we will not include the correction in model applied in this work. We will extend our model by a more general AMF calculation in future studies.

- *Reviewer's comment: p.10,l.203: How did you estimate the background SO2? Your method relies on using the background signal in order to determine the CD in the plume. Which I0 did you use for the determination of the background SO2?*

  Author's response: The SO_2 background signal has no significant impact on the measurement. A plume-free region within the measurement image is used to calculate the differential SO_2 signal induced by the plume (see: revised manuscript lines: 226 - 230). The model is not impacted by the atmospheric SO_2 background, since its absorption does not significantly impact the shape of the solar spectrum in the measurement wavelength range.

1.4 Typos

- p.4,l.80: stratosperhic -> stratospheric
  corrected as proposed

- p.7,l.145: describe -> described
  corrected as proposed

- p.7,l.151: add a comma after "model"
  corrected as proposed

- p.7,l.154: add a comma after "quality" corrected as proposed

- p.7,l.157: including -> include
  corrected as proposed

- p.8,l.173: add a comma after the first "model"
  corrected as proposed

- On several occasions, the form "I. e." is used at the beginning of a sentence (like on p.8, line 177). I don’t understand this abbreviation.
  We changed the abbreviation “I.e.” occurring at the beginning of the sentences either into “In other words” or “That is to say”.

- p.8,l.179: remove the comma after "Note"
  corrected as proposed

- p.10,l.199: start a new paragraph with "An evaluated ..."
  corrected as proposed

- p.11,l.229: "increases selectivity" -> "increases the selectivity"
  corrected as proposed

Author’s response to Review RC2 by Toshiya Mori

First, we like to gratefully thank for the constructive, detailed and helpful comments given by Toshiya Mori. We are convinced that the comments allowed us to improve the manuscript quality within the revision process.

For clarity we answer the specific comments directly (bold printed). The reviewer comment is set in italic font, the authors response in normal font. We added a figure in section 3.3 (Fig. 5 (b)), recalculated the coefficients of Eq. 8, and recalculated the Fig. 7 with new values of Eq. 8. On several occasions we changed and added sentences resulting in minor changes to the manuscript.

"2.2 The IFPICS prototype"

Reviewer’s comment: From Figure 2, it seems that the tilt angles of FPI is controlled by a stepping motor. However, there seems to be no description on how the tilt angles for the two settings A and B are controlled in the manuscript. Although the optics of the IFPICS are explained in detail, the mechanical part of the IFPICS is poorly explained. The mechanical part of the IFPICS prototype especially about the changing of the tilt angle should also be described in the manuscript. How long does it take to change the tilt angle? This may partly explain rather low frame rate of 0.2 Hz for the pair of images.

Author’s response: This is a valid comment. In the revised version we include the mechanical description of the IFPICS prototype:
The tilt angle for the two settings A and B is - as mentioned in the comment - controlled by a stepping motor. The motor has a step resolution of 0.9°. It is equipped with an additional planetary gearbox with a reduction ratio of 1 to 9 reducing the effective step resolution to 0.1°. The motor is controlled by a microcontroller combined with a stepping motor controller. The controller enables the operation of the stepper motor in micro-stepping mode thus further improving the angular resolution by a factor of 16, yielding a final resolution of 0.00625 degrees per motor step. An optical switch is used for position sensing of the stepper motor.
The time required for changing the tilt from setting A to setting B is of the order of 0.15 s. Hence, the low frame rate of the prototype of 0.2 Hz (5.5 seconds per pair of frames) mainly arises from controlling and triggering the employed UV detector.

We changed and extended the sentence: (submitted manuscript lines: 125 - 127):
“The static air-spaced FPI (*d*, *n* and *R* fixed, provided by *SLS Optics Ltd*.) can be tilted within the parallelised light path in order to tune its spectral transmission T^{eff}_{FPI} between setting A and B via variation of the incidence angle α (see Section 2.1).”

To (revised manuscript lines: 135 - 138):
“The FPI is the central optical element of the IFPICS prototype and is implemented as static air-spaced etalon with fixed *d, n*, and *R* (provided by *SLS Optics Ltd*.). The mirrors are separated using ultra low expansion glass spacers to maintain a constant mirror separation *d* and parallelism over the large clear aperture of 20 mm even in variable environmental conditions. In order to tune the spectral transmission $\mathrm{T^{eff}_{FPI}}$ between setting A and B a variation of the incidence angle α is applied.”

We added the sentence: (revised manuscript lines: 138 - 141):
"The FPI can be tilted within the parallelised light path using a stepper motor. The stepper motor has a resolution of 0.9° per step, is equipped with a planetary gearbox (reduction rate 1/9) and operated in micro-stepping mode (1/16) resulting in a resolution of 0.00625°per motor step. The time required for tilting between our settings A and B is ≈ 0.15 s."

Table 1 and Equation 6
Reviewer's comment: Direct use of the parameter values in Table 1 into equation 6 seems inappropriate. Either the values in Table 1 or the equation 6 needed to be modified. The sine in eq. 6 is in radiance and the cosine is in degree. They should be matched. d and λ in eq. 6 needed to be in the same unit or conversion factor should be included in eq. 6.

Author's response: Thanks for that comment. We will include a note for the units required for sine and cosine calculation. For d and λ the units of μm and nm are indicated in Tab. 1.

We added the footnote to Tab. 1:
"*: used in units of radian in the instrument model Eq. 6 & 7"

Figure 6
Reviewer's comment: In Fig.6(b), CD S_{SO2} value between Row 400 and 415 (most part is hidden behind the "crater flank" label) seems to be shifted to positive side unlike those of other Rows (distributed around zero). As stated in the end of the figure caption of Fig. 5, IA is basically equal to IB for both background sky and flank. Is there any possibility of SO2 on the flank or is there any other reason to explain for the positive shift? According to a Global Volcanism Program report in "Global Volcanism Program, 2019. Report on Etna (Italy) (Crafford, A.E., and Venzke, E., eds.). Bulletin of the Global Volcanism Network, 44:10. Smithsonian Institution. https://doi.org/10.5479/si.GVP.BGVN201910-211060." There was a lava flow event between 19-21 July, 2019 (until a day before the observation) on the eastern flank of SEC. Probably part of the flow may have been in the view of the IFPICS at the time of the observation on 22 July, 2019. Is there any possibility detecting volcanic fume with SO2 from the lava flow?

Author's response: Yes, indeed there was a lava flow event at Mt. Etna close to the time we were measuring. However, we do not expect to detect its fume. The enhanced signal can most likely be explained by the low level of light scattered from the crater flank and the thereby increasing influence of hardware systematics of the detector and statistical fluctuations.

Lines 194-200:" The SZA during the time of the measurement is (78±3) (NOAA) witha VCDO3retrieved calibration function...with $x0 = 1.0\times10^{13}$, $x1 = 1.1\times10^{19}$, $x2 =9.3\times10^{18}$, $x3 = 7.9\times10^{18}$, and $x4 = 1.6\times10^{19}$in units of molec cm^{-2} respectively."
Reviewer's comment: Reading here and the figure caption of Fig. 6, x0-x4 parameters is supposed to correspond to SZA=78 degrees. As I plotted Eq. 8 with

x0-x4 values, it seems the conversion function correspond to SZA 25 degrees. Please give the parameters for SZA=78 degrees corresponding to the observation. If the conversion function withx0-x4 given in the manuscript are used for calculation of SO2 CD distributions in Fig.6, SO2CD need to be recalculated using appropriate conversion function.

Author’s response: Yes, the given polynomial parameters accidentally corresponded to an SZA of 25 degrees. However, it was only a copy error of from the model code values into the manuscript. All calculations were performed with the correct calibration function as given in the following:
x0 = 1.04 ×10^{13}, x1 = 1.81×10^{19}, x2 =1.73×10^{19}, x3 = 1.69×10^{18}, and x4 = 6.77×10^{19}.

Equation 8

Reviewer’s comment: According to equation 1, AA is zero, if SO2 CD (S) is zero. Considering this,0th order parameter x0 may not be needed or may be set to zero in the 4th order polynomial fitting.

Author’s response: Yes, that is true as we retrieve the calibration function from a numerical model. We changed our polynomial fitting using a y-intercept fixed to zero. The new calibration function reads:
x0 = 0, x1 = 1.81×10^{19}, x2 =1.72×10^{19}, x3 = 1.73×10^{19}, and x4 = 6.64×10^{19}.
We recalculated Fig. 6 (now Fig. 7) using the new calibration function. The changes are marginal and slightly visible in the noise of the crater flank in Fig. 7 (b).

We changed the sentence (submitted manuscript line: 197 - 198):
“[…] with x0 = 1.0×10^{13}, x1 = 1.1×10^{19}, x2 =9.3×10^{19}, x3 = 7.9×10^{18}, and x4 = 1.6×10^{19} in units of molec cm^{-2} respectively.”

To (revised manuscript lines: 219 - 220):
“[…] with x0 = 0, x1 = 1.8×10^{19}, x2 =1.7×10^{19}, x3 = 1.7×10^{19}, and x4 = 6.6×10^{19} in units of molec cm^{-2} respectively with x0 fixed to zero.”

We recalculated Fig. 6 (revised manuscript Fig. 7):

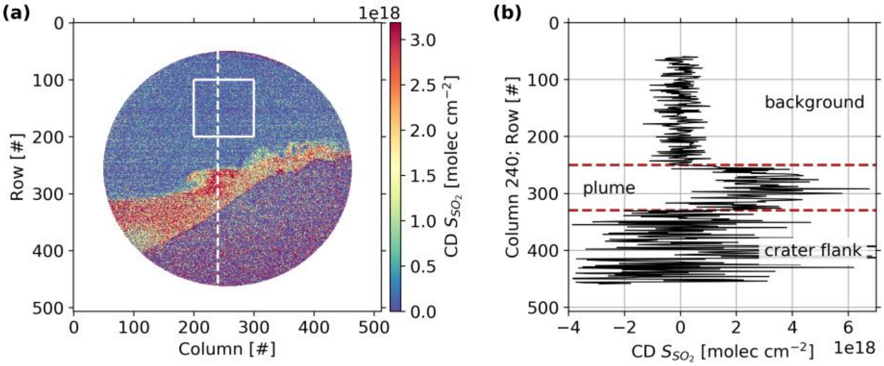

Figure 7. (a): Volcanic plume SO_2 CD distribution calculated from images acquired with the IFPICS prototype and using the instrument forward model conversion function $S_{SO2}(\tilde{\tau})$ (see Eq. 8). The plume free area indicated by a white square (100 x 100 pixel) is used to correct for atmospheric background and to obtain an estimation for the detection limit. **(b):** Individual SO_2 CD column 240 (indicated by dashed white line in (a)) showing that background, plume, and crater flank region are clearly distinguishable. High scattering in the crater flank region is induced by low radiance.

Line 203:" The atmospheric background is $S_{SO2,bg}$= 4.3×10^{16}molec cm^{-2}"

Reviewer's comment: *Definition of atmospheric background S_{SO2} is not clear. Does this value correspond to the difference of S_{SO2} between plume direction and flat-field image direction or to the absolute atmospheric background value for observation direction?*

Author's response: Thanks for that comment, we shall clarify the definition of the atmospheric background $S_{SO2,bg}$ in the revised manuscript:
The $S_{SO2,bg}$ accounts for the difference in S_{SO2} between the plume direction and flat-field image direction.

We added the sentence (revised manuscript lines: 227 - 229):
"Since the $S_{SO2,bg}$ is determined from an evaluated CD distribution image it accounts for the residual signal in S_{SO2} between the direction of the volcanic plume and the direction of the flat-field images used in the evaluation."

Lines 230-231: "Furthermore, the small interference to broadband effects extends the range of meteorological conditions acceptable for field measurement.

Reviewer's comment: *I agree that one of the major advantages of the IFPICS is extension of acceptable meteorological ranges in the field measurements such as minimal influence of background clouds. I suppose the author need to explain more specific on this. Personally, I feel slightly pity because the authors did not show clear example images corresponding to outcome of "the small interference to broadband effects" in this manuscript, which would definitely convince the readers of the clear advantages of the new IFPICS compared to the conventional SO2 cameras.*

Author's response: Yes, this is a valid comment. We do expect a weaker influence on broadband interferences for example induced by background clouds in contrast to traditional filter based SO_2 cameras. This statement is based on model calculations as shown in Kuhn et al., 2014. However, within this work our main goal was to demonstrate the feasibility of the IFPICS technique to detect volcanic SO_2 emissions. Hence, in our up to now limited data set we only took data under good weather conditions without background sky clouds. This fact limits our dataset, and unfortunately, we cannot provide exemplary images yet. Despite that fact, we certainly plan to address this topic in near future studies. For this manuscript we will weaken our statement on this topic.

We changed the sentence (submitted manuscript lines: 230 - 231):
"Furthermore, the small interference to broadband effects extends the range of meteorological conditions acceptable for field measurement. "

To (revised manuscript lines: 282 - 284):
"Furthermore, the expected smaller interference to broadband effects in comparison to traditional SO_2 imaging techniques should allow to extend the range of meteorological conditions acceptable for field measurement (see Kuhn et al., 2014). "

Minor comments:

- **Line 190: “The circular shape of the retrieved image arises from the FPI’s circular clear aperture limiting the imaging FOV.” And line 216:” a high spatial and temporal resolution (400×400 pixel, 1 s integration time)”**
  Reviewer’s comment: The 2D UV-sensitive CMOS sensor (SCM2020-UV) is originally a 2000x2000 pixels sensor. It seems 4x4 pixel binning is applied to the images. If so, please indicate in the manuscript.

  Author’s response: Yes, indeed. We applied 4x4 pixel binning and will include this information in the revised version of the manuscript.

  We changed the sentence (submitted manuscript lines: 117 - 118):
  “A 2D UV-sensitive CMOS sensor (SCM2020-UV provided by *EHD imaging*) is used to acquire images.”

  To (revised manuscript lines: 125 - 126):
  “A 2D UV-sensitive CMOS sensor (SCM2020-UV provided by *EHD imaging*) is used to acquire images. The sensor is operated in 4x4 binning mode yielding a final image resolution of 512x512pixel.”

  We changed the sentence (submitted manuscript lines: 215 – 216):
  “We were able to unequivocally resolve the dynamical evolution of SO_2 in a volcanic plume with a high spatial and temporal resolution (400x400 pixel, 1 s integration time).”

  To: (revised manuscript lines: 262 - 263):
  “We were able to unequivocally resolve the dynamical evolution of SO_2 in a volcanic plume with a high spatial and temporal resolution (400x400 pixel, 1 s integration time, 4x4 binning).”

  We changed the sentence (submitted manuscript line: 149):
  “The exposure time was set to 1 s for all acquired images.”

  To (revised manuscript lines: 167 - 169):
  “The exposure time was set to 1 s for all measurements and 4x4 binning (total spatial resolution of 512x512 pixels) was applied to all acquired images.”

- **Lines 205-207:” The similar plume free area (white square, 100×100 pixel, in Fig.6, (a)) is further used to give an estimation for the SO2 detection limit of the IFPICS prototype by calculating the 1-σ pixel-pixel standard deviation. The obtained detection limit is 5.5×10^{17}molec $cm^{-2}s^{-1/2}$given by the noise equivalent signal.”**
  Reviewer’s comment: Please explain how the detection limit was calculated more in detail. 1-sigma pixel-pixel standard deviation does not seem to give the detection limit unit indicated here.

  Author’s response: Thank you for this comment. We used the 100x100 pixel area and calculated the respective standard deviation for these pixel. This yields the stated detection limit of 5.5×10^{17}molec cm^{-2}. The unit of $s^{-1/2}$ arises from the time dependency of the photon shot noise which is proportional to 1/sqrt(t) with the exposure time t. As the images have been obtained with an exposure time of 1s the unit of $s^{-1/2}$ can be included. We will clarify this statement in the revised manuscript:

We changed the sentence (submitted manuscript line: 207):
“The obtained detection limit is 5.5×10^{17}molec cm^{-2} $s^{-1/2}$ given by the noise equivalent signal.”

To (revised manuscript lines: 231 - 232):
“The obtained detection limit for an exposure time of one second is 5.5×10^{17} molec cm^{-2} given by the noise equivalent signal. “

- **Figure caption of Fig. A1:” acquired with the IFPICS prototype on 22. July 2019, 08:50- 09:10 CET”**
  Delete “.” after “on 22”
  Corrected as proposed

Other comment:
<u>Reviewer’s comment</u>: It would be helpful, especially for non-volcanological readers, to show visual image of the plume from the observation site if available.

<u>Author’s response</u>: We added a visual image to Fig. 4 (revised manuscript: Fig. 5).

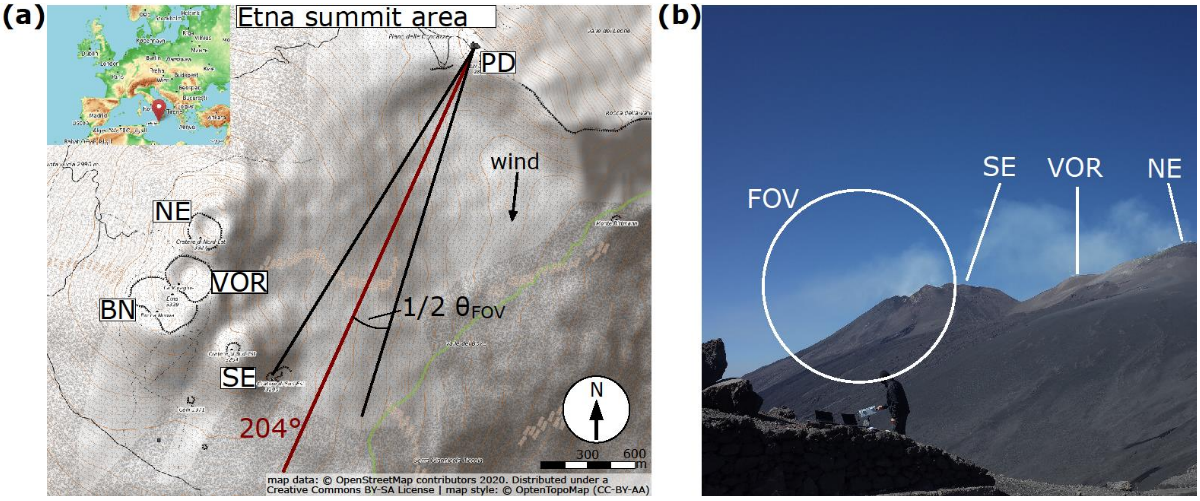

map data: © OpenStreetMap contributors 2020. Distributed under a Creative Commons BY-SA License | map style: © OptenTopoMap (CC-BY-AA)

Figure 5. (a): Topographic map of the Mt. Etna summit area, North East crater (NE), Voragine (VOR), Bocca Nuova (BN), South East crater (SE) and measurement location at the Osservatorio Vulcanologico Pizzi Deneri (PD) are indicated. The viewing direction on 22 July 2019 is 204° (red drawn) with an FOV of $\theta = 18°$ (black drawn) and an elevation of 5°. The FOV is partly covering the plume emanating from SE crater. The average wind direction is ≈5° with a speed of ≈ 6 m s^{-1} (wind data from UWYO). **(b)**: Visual image of the volcanic plume on 22 July 2019 with indicated camera field of view (FOV).

Quantitative imaging of volcanic SO_2 plumes with Fabry Pérot Interferometer Correlation Spectroscopy

Christopher Fuchs[1], Jonas Kuhn[1,2], Nicole Bobrowski[1,2], and Ulrich Platt[1,2]

[1]Institute of Environmental Physics, University of Heidelberg, Germany
[2]Max Planck Institute for Chemistry, Mainz, Germany

Correspondence: C. Fuchs (cfuchs@iup.uni-heidelberg.de), J. Kuhn (jkuhn@iup.uni-heidelberg.de)

Abstract. We present first measurements with a novel imaging technique for atmospheric trace gases in the UV spectral range. Imaging Fabry Pérot Interferometer Correlation Spectroscopy (IFPICS), employs a Fabry Pérot Interferometer (FPI) as wavelength selective element. Matching the FPIs distinct, periodic transmission features to the characteristic differential absorption structures of the investigated trace gas allows to measure differential atmospheric column density (CD) distributions of numerous trace gases ~~, e.g. sulphur dioxide (SO_2), bromine monoxide (BrO), or nitrogen dioxide (NO_2), with high spatial and temporal resolution.~~ with high spatial and temporal resolution. Here we demonstrate measurements of sulphur dioxide (SO2) while earlier model calculations show that bromine monoxide (BrO) and nitrogen dioxide (NO2) are also possible.The high specificity in the spectral detection of IFPICS minimises cross interferences to other trace gases and aerosol extinction allowing precise determination of gas fluxes. Furthermore, the instrument response can be modelled using absorption cross sections and a solar atlas spectrum from the literature, thereby avoiding additional calibration procedures, e.g. using gas cells. In a field campaign, we recorded the temporal CD evolution of SO_2 in the volcanic plume of Mt. Etna with an ~~integration~~ exposure time of $1\,\mathrm{s}$ ~~,~~and 400×400 pixels spatial resolution. The ~~first IFPICS prototype can reach~~ temporal resolution of the time series was limited by the available non-ideal prototype hardware to about $5.5\,\mathrm{s}$. Nevertheless, a detection limit of ~~$2.1 \times 10^{17}\,\mathrm{molec\,cm^{-2}\,s^{-1/2}}$~~$2.1 \times 10^{17}\,\mathrm{molec\,cm^{-2}}$ could be reached, which is comparable to traditional and much less selective volcanic SO_2 imaging techniques.

1 Introduction

Ground based imaging of atmospheric trace gas distributions has a great potential to give new insights into mixing processes and chemical conversion of atmospheric trace gases by allowing their observation at high spatio-temporal resolution. Whereas present space borne trace gas imaging provides daily global coverage with a spatial resolution of a few km (e.g. Veefkind et al., 2012), ground based observation can potentially reach a spatial resolution in the order of metres and a temporal resolution in the single digit Hz range. Such techniques in particular allow the investigation of trace gas distributions with strong gradients and short time scale chemical conversions.

There are several approaches for imaging trace gas distributions using scattered sunlight in the UV-Vis wavelength range (see e.g. Platt and Stutz, 2008; Platt et al., 2015): An image can be scanned pixel by pixel with a telescope and recorded spectra are evaluated to determine the trace gas column density (whiskbroom approach). Alternatively, with a more complex optics and a two dimensional detector, one detector dimension of the spectrograph can be used for spatially resolving an image column. Column by column (or pushbroom) scanning then resolves an image. ~~A third approach applies a small number of (typically two) wavelength channels by using wavelength selective optical elements for the entire image frame, thereby usually strongly reducing the spectral resolution (e.g. Mori and Burton, 2006; Dekemper et al., 2016).~~ The high spectral resolution of the ~~first two approaches~~ spectrograph based techniques allows the accurate and simultaneous identification of several trace gases, however, the light throughput and the scanning process severely limit the temporal resolution. ~~The third approach can~~ A third approach applies tunable filters to resolve the trace gas spectral features, e.g. acousto-optical tunable filter (Dekemper et al., 2016), as wavelength selective elements for an entire image frame. The application of tunable filters can have high spectral resolution and hence high trace gas selectivity, however, due to limited light throughput the temporal resolution lies in the order of minutes. A fourth imaging technique uses a small number (typically two) wavelength channels selected by static filters, e.g. interference filters (Mori and Burton, 2006). This approach can be quite fast with a temporal resolution in the order of seconds, the trace gas selectivity, however, strongly depends on the correlation of trace gas absorption with the wavelength selective elements and usually is rather marginal.

Fabry Pérot Interferometers (FPIs) exhibit a periodic spectral transmission pattern, which can be matched to periodic spectral features (typically due to rotational or vibrational structures of electronic transitions) of the trace gas absorption, thereby yielding very high correlation for some trace gases. Imaging Fabry Pérot Interferometer Correlation Spectroscopy (IFPICS) thus essentially combines the advantage of fast image acquisition with selective spectral identification of the target trace gas. IFPICS was proposed by Kuhn et al. (2014) and discussed in Platt et al. (2015) for volcanic $\mathrm{SO_2}$. Kuhn et al. (2019) demonstrated the feasibility with a one-pixel prototype for volcanic $\mathrm{SO_2}$ and evaluated its applicability to other trace gases.

Here we present first imaging measurements (at a resolution of 400×400 pixels, $1\,\mathrm{s}$ exposure time) performed with IFPICS and confirm its high selectivity and sensitivity. A prototype instrument for $\mathrm{SO_2}$ was tested at Mt. Etna volcano, Italy, showing a noise equivalent signal between $2.1\times10^{17} - 5.5\times10^{17}\,\mathrm{molec\,cm^{-2}\,s^{-1/2}}$. Furthermore, we show that the instrument response can be modelled and thereby intrinsically calibrated, using a solar atlas spectrum and literature trace gas absorption cross sections.

Existing interference filter based $\mathrm{SO_2}$ cameras used for e.g. the quantification of volcanic trace gas emission fluxes into the atmosphere (Mori and Burton, 2006; Bluth et al., 2007; Kern et al., 2015a), exhibit strong cross interferences to aerosol scattering extinction and other trace gases (Lübcke et al., 2013; Kuhn et al., 2014). Furthermore, these techniques require in field calibration. Besides the thereby induced systematic errors that propagate into the emission flux quantification, the detection limit is mostly determined by these cross interferences. Thus, the applicability of the technique is limited to strong emitters with respective plume and weather conditions. The much higher selectivity of IFPICS largely extends the range of applicable conditions (e.g. to ship emissions and weaker emitting volcanoes) and significantly reduces the systematic errors. Furthermore, the extension of the technique to other trace gases e.g. bromine monoxide (BrO), formaldehyde (HCHO) or nitrogen dioxide ($\mathrm{NO_2}$) can give new important insights into short scale chemical conversion processes in the atmosphere.

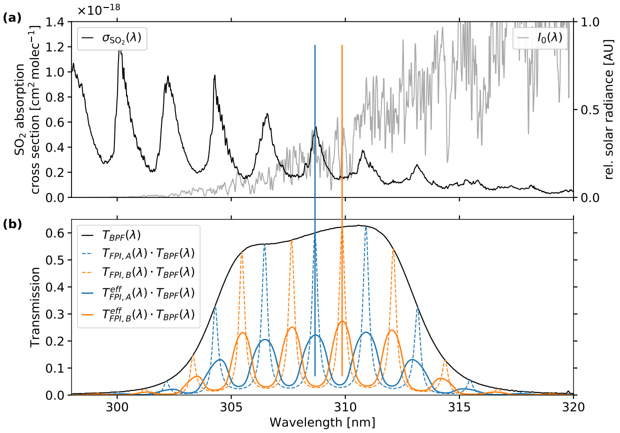

Figure 1. Spectral variation of: **(a)** The $\mathrm{SO_2}$ absorption cross section $\sigma_{\mathrm{SO_2}}$ (black drawn, left axis, according to Bogumil et al. (2003)) and the scattered skylight radiance $I_0(\lambda)$ (gray drawn, right axis in relative units), given by Eq. 2. **(b)** The FPI transmissions in settings A and B yielding the maximum AA detectable (best correlation/anti-correlation to $\sigma_{\mathrm{SO_2}}$) in the spectral range specified by the used band pass filter (BPF). Shown are: The BPF transmission $T_{BPF}(\lambda)$ (black) and the FPI transmission spectrum for a single beam approach according to Eq. 6 in on-band $T_{FPI,A}(\lambda)$ (dashed blue, correlation with $\sigma_{\mathrm{SO_2}}$) and off-band $T_{FPI,B}(\lambda)$ setting (dashed orange, anti-correlation with $\sigma_{\mathrm{SO_2}}$). The effective FPI transmission spectrum including an incident angle distribution according to Eq. 7 in on-band $T^{eff}_{FPI,A}(\lambda)$(drawn blue) and off-band $T^{eff}_{FPI,B}(\lambda)$ setting (drawn orange).

2 Imaging Fabry Pérot Interferometer Correlation Spectroscopy (IFPICS)

Similarly to the $\mathrm{SO_2}$ camera principle (e.g. Mori and Burton, 2006; Bluth et al., 2007), IFPICS uses an apparent absorbance (AA) $\tilde{\tau} = \tau_A - \tau_B$, i.e. the difference between two measured optical densities τ_A and τ_B, to quantify the column density (CD) $S = \int_0^L c(l)\,\mathrm{d}l$, i.e. the integrated concentration c of the measured gas along a light path L for each pixel of the image. The AA is calculated from two (or more) spectral settings that yield a maximum correlation difference to the gas absorption spectrum. Ideally the periodicity of the FPI fringes are matched to periodic spectral absorption features as shown in Fig. 1 for $\mathrm{SO_2}$. For IFPICS we use two spectral settings A and B. Setting A exhibits on-band absorption, where the FPI transmission maxima coincide with the $\mathrm{SO_2}$ absorption maxima and hence correlating with the differential absorption structures of $\mathrm{SO_2}$. Setting B, uses an off-band position where the FPI transmission maxima anti-correlate with the differential $\mathrm{SO_2}$ absorption structures (see Fig. 1). The spectral separation between setting A and B is thereby reduced by a factor of ≈ 30 (in the case of $\mathrm{SO_2}$) to only $\approx 0.5\,\mathrm{nm}$ in contrast to $\approx 10-15\,\mathrm{nm}$ for traditional $\mathrm{SO_2}$ cameras (see Lübcke et al., 2013; Kern et al., 2015a), which minimises broad band interferences due to e.g. scattering and extinction by aerosols or other absorbing gases. This application of an FPI is similar to approaches reported by Wilson et al. (2007) and Vargas-Rodríguez and Rutt (2009), for the detection of carbon monoxide, carbon dioxide and methane in the infrared spectral range.

By measuring the optical density $\tau_A = \ln(I_A/I_{0,A})$ and $\tau_B = \ln(I_B/I_{0,B})$ in both spectral settings A and B respectively, the relation between the AA $\tilde{\tau}(S)$ with the CD S is given by

$$\tilde{\tau}(S) = \tau_A - \tau_B = -\log\frac{I_A}{I_{0,A}} + \log\frac{I_B}{I_{0,B}} = k(S) = \Delta\tilde{\sigma}(S)\cdot S, \tag{1}$$

where I_A, I_B denote the radiances with and $I_{0,A}$, $I_{0,B}$ the radiance without the presence of the target trace gas in the absorption light path. The absorber free reference radiances $I_{0,A}$ and $I_{0,B}$ can be determined from e.g. a reference region within the image. The differential weighted effective trace gas absorption cross section $\Delta\tilde{\sigma}(S)$ becomes independent of S for small AAs ($\tilde{\tau} \ll 1$). At higher AAs saturation effects occur due to the non-linearity of Lambert-Beer's law, however knowledge of the absorption cross sections, the background radiation spectrum, and the instrument transmission allows to calculate $\tilde{\tau}$ for arbitrary CDs S using a numerical model.

2.1 Instrument model

The AA $\tilde{\tau}$ is modelled for given target trace gas CDs S by simulating the incoming radiances I_A, I_B and $I_{0,A}$, $I_{0,B}$. As incident radiation a high-resolution, top of atmosphere (TOA) solar atlas spectrum $I_{0,TOA}(\lambda)$ is used according to Chance and Kurucz (2010). The TOA spectrum is scaled by the wavelength λ^{-4} approximating a Rayleigh scattering atmosphere. Since our measurement wavelength range, of 304-313 nm for SO_2, overlaps with absorption of ozone (O_3), the TOA spectrum is corrected for the ~~stratosperhic~~ stratospheric O_3 absorption by multiplying all intensities with the Lambert-Beer's term $e^{-\sigma_{O_3}(\lambda)\cdot S_{O_3}}$. Where S_{O_3} denotes the total atmospheric ozone slant column density, e.g. according to TEMIS Database, (Veefkind et al., 2006), and σ_{O_3} the O_3 absorption cross section according to Serdyuchenko et al. (2014). This yields the scattered skylight radiance $I_0(\lambda)$

$$I_0(\lambda) = I_{0,TOA}(\lambda)\cdot e^{-\sigma_{O_3}(\lambda)\cdot S_{O_3}}\cdot f(\lambda^{-4})\cancel{.}, \tag{2}$$

indicated in Fig. 2. Based on $I_0(\lambda)$ the radiances measured by the instrument for the two respective spectral settings are calculated with the absorption of trace gases and the spectral instrument transfer function $T_{instr}(\lambda)$. The investigated target trace gas j (in this work SO_2) and potentially interfering trace gas species k (in this work O_3) are added according to Lambert-Beer's law. In the following we use the index i, denoting the FPI settings A and B, respectively. The quantity $I_{0,i}$ thereby denotes the reference radiance excluding the target trace gas j from the light path ~~.~~ (see Fig. 2).

$$I_i = \int \mathrm{d}\lambda\, I_0(\lambda)\cdot\exp\left(-\sigma_j(\lambda)\,S_j - \sum_k \sigma_k(\lambda)\,S_k\right)\cdot T_{instr,i}(\lambda) \tag{3}$$

$$I_{0,i} = \int \mathrm{d}\lambda\, I_0(\lambda)\cdot\exp\left(-\sum_k \sigma_k(\lambda)\,S_k\right)\cdot T_{instr,i}(\lambda) \tag{4}$$

The spectral instrument transfer functions $T_{instr,i}(\lambda)$ for the two spectral settings

$$T_{instr,i}(\lambda) = T^{eff}_{FPI,i}(\lambda)\cdot T_{BPF}(\lambda)\cdot Q(\lambda)\cdot\eta(\lambda) \tag{5}$$

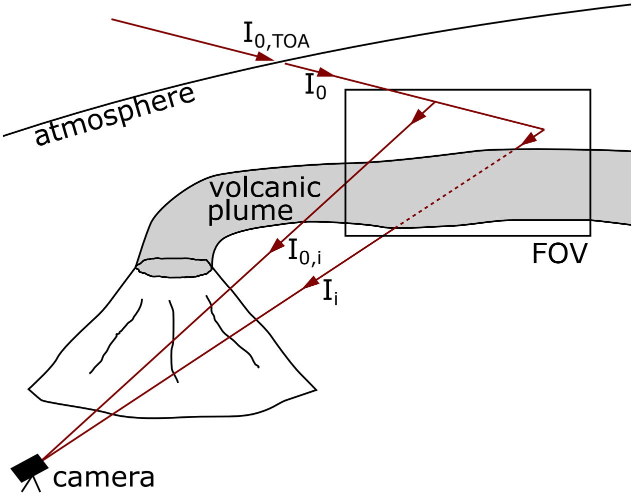

Figure 2. Schematic of the IFPICS measurement geometry including the simulated radiances used in the instrument model. The incident top of atmosphere (TOA) radiation $I_{0,TOA}$ is propagating through the atmosphere and is potentially scattered into the IFPICS camera field of view (FOV) yielding the scattered skylight radiance I_0. The camera records radiation in the respective FPI settings $i =$ A and B that either traverses the volcanic plume I_i or originates from a plume free area within the FOV $I_{0,i}$.

consists of the measured band pass filter (BPF) transmission spectrum $T_{BPF}(\lambda)$, the spectral (i.e. wavelength dependent) quantum efficiency $Q(\lambda)$ of the detector, and a spectral loss factor $\eta(\lambda)$ of the employed optical components (e.g. by reflections). Considering only a single, parallel beam of light traversing the instrument the FPI transmission spectrum $T_{FPI,i}(\lambda)$ is defined by the Airy function (Perot and Fabry, 1899)

$$T_{FPI,i}(\lambda;\alpha_i,d,n,R) = \left[1 + \frac{4\cdot R}{(1-R)^2}\cdot\sin^2\left(\frac{2\pi\cdot d\cdot n\cdot\cos\alpha_i}{\lambda}\right)\right]^{-1} \tag{6}$$

with the light beam incidence angle α_i for the two spectral settings onto the FPI, the FPI mirror separation d, the refractive index n of the medium inside the FPI, and the FPI reflectivity R (see Tab. 1, Fig. 1 and Fig. 3, (~~e~~d)). The FPI used in this work is static and air-spaced, meaning d, n, and R are fixed. Hence, the incidence angle α_i is the exclusive free parameter available to tune the FPIs transmission spectrum $T_{FPI,i}$ between settings $i =$ A and $i =$ B respectively. The change in α_i is achieved by tilting the FPI optical axis with respect to the imaging optical axis (see Section 2.2).

However, in reality a spectral setting will always contain a range of incidence angles onto the FPI. In this work we assume cone shaped light beams, with half cone opening angles ω_c, where the entire cone can be tilted by α_i relative to the normal of the FPI mirrors (see Fig. 3, (~~e~~d)). From this assumption follows that the incidence angles α_i are distributed over a cone with the incidence angle distribution $\gamma(\alpha_i,\omega_c,\vartheta,\varphi)$, where ϑ and φ are the polar and azimuth angles, respectively. Hence, the single beam FPI transmission spectrum $T_{FPI,i}(\lambda)$ of ~~Equation~~ Eq. 6 is extended by a weighted average over

$T_{FPI,i}(\lambda;\gamma(\alpha_i,\omega_c,\vartheta,\varphi),d,n,R)$, giving the effective FPI transmission spectrum $T^{eff}_{FPI,i}(\lambda)$

$$T^{eff}_{FPI,i}(\lambda;\gamma(\alpha_i,\omega_c),d,n,R) = \frac{1}{N(\gamma(\alpha_i,\omega_c))}\int\limits_{0}^{\varphi_{max}}\int\limits_{\vartheta_{min}}^{\vartheta_{max}} T_{FPI,i}(\lambda;\gamma(\alpha_i,\omega_c,\vartheta,\varphi),d,n,R)\sin\vartheta\,\mathrm{d}\vartheta\,\mathrm{d}\varphi. \tag{7}$$

Thereby, $N(\gamma(\alpha_i,\omega_c))$ denotes the weighting function with $N(\gamma(\alpha_i,\omega_c)) = \int_0^{\varphi_{max}}\int_{\vartheta_{min}}^{\vartheta_{max}}\sin\vartheta\,\mathrm{d}\vartheta\,\mathrm{d}\varphi$ given by integral in Eq. 7 excluding the integrand $T_{FPI,i}$ itself, ϑ the polar angle and φ the azimuth angle of the spherical integration within boundaries defined by the tilted cone shaped light beams. E.g.: for a non-tilted FPI ($\alpha_i = 0$) the integration boundaries are $\vartheta \in [0,\omega_c]$ and $\varphi \in [0,2\pi]$, for a tilted FPI however, the transformation of $\gamma(\alpha_i,\omega_c,\vartheta,\varphi)$ is more complex and requires several case analyses. The incidence angle distribution $\gamma(\alpha_i,\omega_c)$ will affect the shape of the FPI transmission spectrum by decreasing the effective finesse F of the FPI leading to a blurring of the FPI fringes (see Fig. 1).

2.2 The IFPICS prototype

The IFPICS prototype is a newly developed instrument, designed to function under harsh environmental conditions in remote locations like e.g. in the proximity to volcanoes. Hence, the prototype is designed to be small with dimensions of $200\,\mathrm{mm}\times 350\,\mathrm{mm}\times 130\,\mathrm{mm}$, lightweight with 4.8 kg (see Fig. 3, (a)) and has a power consumption $< 10\,\mathrm{W}$, thus can be battery-operated for several hours. A 2D UV-sensitive CMOS sensor with 2048×2048 pixel resolution (SCM2020-UV provided by *EHD imaging*) is used to acquire images. The sensor is operated in 4×4 binning mode yielding a final image resolution of512×512 pixel. However, we found that the software of the SCM2020-UV image sensor does not allow sufficiently precise triggering. Therefore ≈ 0.6 seconds are lost in each image acquisition, which severely limits the operation of the IFPICS camera. Replacement of the sensor by a scientific-grade UV detector array will solve this problem in future studies.

The internal camera optics is highly modular and easily adjustable. The IFPICS prototype employs an image side telecentric optical setup as proposed in Kuhn et al. (2014, 2019). A photograph and a schematic drawing are shown in Fig. 3. An aperture and a lens (lens 1) parallelise incoming light from the imaging field of view (FOV) before it traverses the FPI and the BPF. A second lens (lens 2) focusses the light onto the 2D UV-sensitive sensor. Thereby, in good approximation, all the pixels of the image experience the same spectral instrument transfer function $T_{instr,i}(\lambda)$ for the two wavelength settings.~~The static air-spaced FPI (d, n and R fixed, provided by *SLS Optics Ltd.*) can be tilted within the parallelised light path in order to tune its spectral transmission T^{eff}_{FPI} between setting A and B via variation of the incidence angle α (see Section 2.1).~~

The FPI is the central optical element of the IFPICS prototype and is implemented as static air-spaced etalon with fixed d, n, and R (provided by *SLS Optics Ltd.*). The mirrors are separated using ultra low expansion glass spacers to maintain a constant mirror separation d and parallelism over the large clear aperture of $20\,\mathrm{mm}$ even in variable environmental conditions. In order to tune the spectral transmission T^{eff}_{FPI} between setting A and B a variation of the incidence angle α is applied. The FPI can be tilted within the parallelised light path using a stepper motor. The stepper motor has a resolution of 0.9° per step, is equipped with a planetary gearbox (reduction rate 1/9) and operated in micro-stepping mode (1/16) resulting in a resolution of 0.00625° per motor step. The time required for tilting between our settings A and B is $\approx 0.15\,\mathrm{s}$. We favour the approach of tilting the FPI over changing internal physical properties like, e.g. the mirror separation d by piezoelectric actuators, as it keeps simplicity,

Table 1. Parameters of the optical components installed in the IFPICS prototype and used in the calibration model. The uncertainties of the model input parameters are shown.

parameter	value	uncertainties	description
d [μm]	21.666	$\pm$ 0.002	FPI plate separation
R	0.65		FPI reflectivity
F	7.15		FPI finesse
n	1.0003		refractive index (air)
α_A [°]	8.17*	$\pm$ 0.02	FPI tilt, on-band
α_B [°]	6.45*	$\pm$ 0.02	FPI tilt, off-band
$T_{BPF,max}$	0.63		BPF peak transmission
λ_{BPF} [nm]	308.5		BPF central wavelength
δ_{BPF} [nm]	9.0		BPF FWHM
f [mm]	47†	$\pm$ 2	lens 1 focal length~~*~~
a [mm]	1.55	$\pm$ 0.05	aperture diameter
ω_c [°]	0.945		half cone opening angle
θ_{FOV} [°]	18		imaging FOV

*: used in units of radian in the instrument model Eq. 6 & 7

†: two lenses: $f = \frac{f_1 \cdot f_2}{f_1 + f_2}$ with $f_1 = f_2 \approx 94\,\mathrm{mm}$ @ $\lambda = 310$ nm

robustness, and accuracy high for measurements under non-laboratory conditions. However it needs to be considered, that the tilting of the FPI will generate a linear shift between the respective images acquired in setting A and B, requiring an alignment in the evaluation process.

The half cone opening angle ω_c is determined by the entrance aperture a and the focal length f of lens 1 and can be calculated by $\omega_c = \arctan(a/2f)$. The physical properties of the optical components and the instrument are listed in Tab. 1 and were mostly chosen according to the dimensioning assumed in the calculations of Kuhn et al. (2019).

The FPI design with fixed d, n and R (see Fig. 3, (c)) in particular is chosen to inherently generate a transmission spectrum matching the differential absorption structures of SO_2. This includes the basic idea that the untilted FPI ($\alpha_i = 0°$) already matches the on-band position A. In our case however, the manufacturing accuracy of d lies within one free spectral range ($\approx 2\,\mathrm{nm}$ for SO_2) yielding that $\alpha_B = 0°$, corresponds to a off-band (B) position ($T^{eff}_{FPI,B}$) and the on-band (A) position ($T^{eff}_{FPI,A}$) is reached by a small tilt of $\alpha_A = 4.5°$. The basic advantages of using small incident angles α_i are, that they keep the spread of the incidence angle distribution $\gamma(\alpha_i, \omega_c)$ (see Section 2.1) low and thereby retain the FPIs effective finesse F high (since the reflectivity R of the FPI-mirror coating is somewhat dependent on the angle of incidence so is the finesse F). This leads to a much weaker blurring of the FPI fringes in the FPI transmission spectrum $T^{eff}_{FPI,i}$ resulting in a higher sensitivity of the instrument (see Fig. 1). With the prototype setup, however, we encountered disturbing reflections for low FPI incidence angles. For that reason we used the subsequent correlating order of the FPI transmission with $\alpha_A = 8.17°$ for an on-band and $\alpha_B = 6.45°$ for an off-band setting (see Tab. 1), thereby making a compromise between sensitivity and accurate evaluable images.

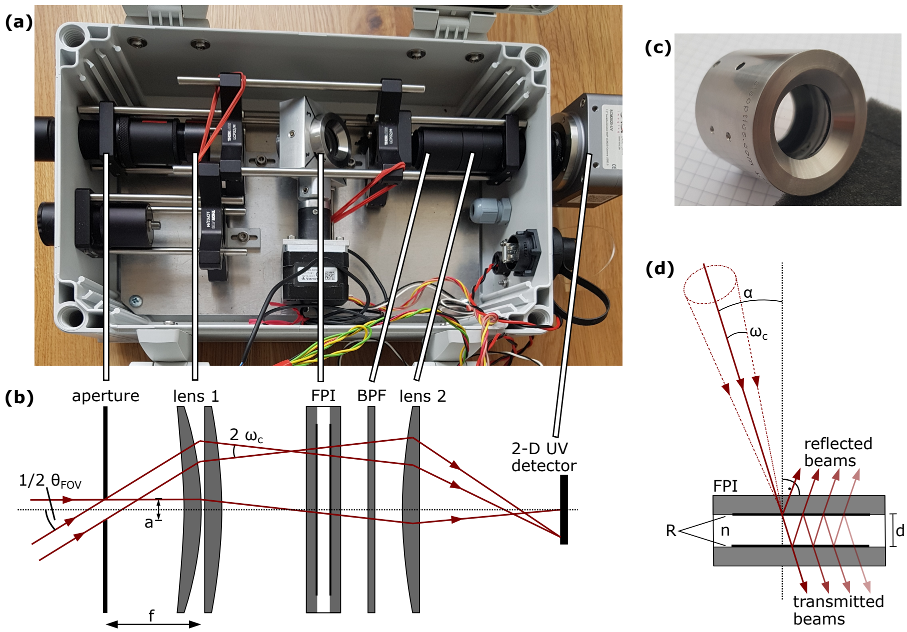

Figure 3. **(a)**: Photograph of the IFPICS instrument. The physical dimensions are $200\,\text{mm} \times 350\,\text{mm} \times 130\,\text{mm}$ (w×l×h) and 4.8 kg. **(b)**: Sketch of the image side telecentric optical setup of the IFPICS prototype. Incident radiation is parallelized by an entrance aperture and lens 1 before traversing the FPI and the band pass filter (BPF). The maximum half cone opening angle ω_c is dependent on the aperture diameter a and the focal length f of lens 1. The camera field of view is $\theta_{FOV} = 18°$. A second lens maps the image onto a 2-D UV sensitive CMOS detector. **(c)**: Photograph of the static air-spaced etalon (FPI) provided by *SLS Optics Ltd.*. **(d)**: Sketch of the FPI. An incoming single beam (drawn red) with incidence angle α is reflected multiple times between the FPI mirrors with reflectance R and separation d. Visualisation of an incoming cone shaped beam (red dash-dotted) with half cone opening angle ω_c and incidence angle α of the cone axis.

3 Proof of concept study

3.1 Measurements at Mt. Etna, Italy

First measurements with the prototype ~~describe~~ described above were performed at the Osservatorio Vulcanologico Pizzi Deneri (lat 37.766, long 15.017, 2800 m a.s.l.) at Mt. Etna, on July 21 and 22, 2019. The physical properties of the IFPICS prototype and the FPI tilt angles α_i for tuning $T^{eff}_{FPI,i}(\lambda)$ between on-band $i = \text{A}$ and off-band setting $i = \text{B}$ were selected according to Tab. 1. The tilt of the FPI generates a linear shift between the recorded on-band and off-band images on the detector and accounts for 6 pixel using tilt angles α_i. This shift needs to be corrected before cross evaluating images recorded in setting A and B. The exposure time was set to 1 s for all measurements and 4×4 binning (total spatial resolution of 512×512 pixels) was applied for all acquired images.

3.2 Validation of the instrument model

To quantify the accuracy of our model, two $\mathrm{SO_2}$ gas cells were measured with the IFPICS prototype and by Differential Optical Absorption Spectroscopy (DOAS, see Platt and Stutz, 2008), on July 21, 2019, 11:10 - 11:20 CET. The sky was used as light source with a constant viewing angle (10° elevation, 270°N azimuth) in a plume free part of the sky. To enhance the image quality, a flat-field correction is used, compensating pixel to pixel variations in sensitivity. The flat-field correction requires the acquisition of dark and flat-field images. The dark images are determined by the arithmetic mean over five images with no light entering the IFPICS instrument and the flat-field images are obtained by the arithmetic mean over five images acquired in a plume free sky region. The flat field images thereby directly ~~including~~ include the reference measurement $I_{0,i}$, making a later correction for the atmospheric background unnecessary. In the same viewing direction I_i is measured for each gas cell and FPI setting i in order to calculate the AA according to Eq. 1. Figure 4 shows the gas cell measurements (red) including uncertainties (error-bars, 1-σ). The uncertainties directly arise from the errors of the DOAS measurement and due to variations in optomechanical settings of the IFPICS prototype.

The instrument model (Eq. 2 - 7) was used to calculate the IFPICSs AA $\tilde{\tau}_{\mathrm{SO_2}}(S_{\mathrm{SO_2}})$ from a given $\mathrm{SO_2}$ CD $S_{\mathrm{SO_2}}$. The model parameters are mostly fixed by the IFPICS prototype optics as given in Tab. 1. The remaining parameter, the atmospheric $\mathrm{O_3}$ slant column density $S_{\mathrm{O_3}}$ (see Eq. 2) is calculated in a geometric approximation $S_{\mathrm{O_3}} = \mathrm{VCD_{O_3}}/\cos(\mathrm{SZA})$ using the solar zentih angle (SZA) and vertical $\mathrm{O_3}$ column density ($\mathrm{VCD_{O_3}}$) which both are location, date and time dependent. They were: SZA $= (53 \pm 3)°$ (according to the solar geometry calculator by NOAA) and $\mathrm{VCD_{O_3}} = (335 \pm 5)\,\mathrm{DU}$ (according to TEMIS database; Veefkind et al., 2006). The $\mathrm{VCD_{O_3}}$ can be treated to be approximately constant over the period of a day.

The output of the instrument model (drawn, black) for an SZA of 53° is shown in Fig. 4. The model uncertainty (shaded grey) is determined by a root mean square over the errors in the output by individually varying the input parameters within their stated uncertainties. The thus calculated calibration function using the instrument model matches the $\mathrm{SO_2}$ gas cells validation measurement within the range of confidence. The model nicely describes the flattening of the AA-CD relation for high CDs (up to $\approx 2.5 \times 10^{18}\,\mathrm{molec\,cm^{-2}}$), which originates from the CD dependence of $\Delta\tilde{\sigma}(S)$ (see Eq. 1).

To show the impacts of the SZA on the instrument model the model output is also calculated for three other SZAs while keeping the other parameters constant. The model output is shown in Fig. 4 for an SZA of 80° (dash-dotted grey) for early morning/late afternoon conditions, SZA of 70° (dashed grey) for morning/afternoon conditions and SZA of 25° (dotted grey) for noon conditions. High SZAs lead to an increase of stratospheric $\mathrm{O_3}$ absorption which alters the spectral shape of the scattered skylight radiance $I_0(\lambda)$ (see Eq. 2) which is used in the forward model. ~~I. e.~~ In other words, for high $\mathrm{O_3}$ absorption, lower wavelength radiance, where the differential $\mathrm{SO_2}$ absorption features are stronger, will contribute less to the integrated radiances I_i, $I_{0,i}$ (Eq. 3, 4). The thereby induced SZA dependence of the sensitivity can easily be accounted for in the model. Note ~~,~~ that this influence of strong $\mathrm{O_3}$ absorption only occurs at our chosen wavelength range for the $\mathrm{SO_2}$ measurement. When applying IFPICS to other trace gases, e.g. BrO or $\mathrm{NO_2}$ at higher wavelength, this effect will be negligible.

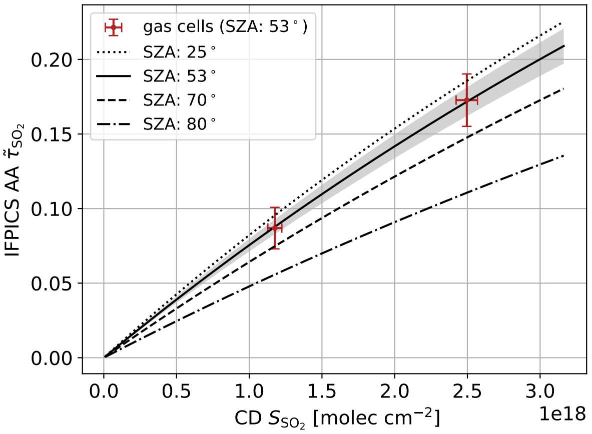

Figure 4. The validation measurement with two SO_2 gas cells (red, with 1-σ error) with the IFPICS prototype and by DOAS on 21 July 2019, 11:10 - 11:20 CET with a solar zenith angle (SZA) of 53°.
The instrument forward model (Eq. 2-7) is used to calculate the IFPICS AA $\tilde{\tau}_{SO_2}$ for a given CD S_{SO_2} range. The model input parameters are shown in Tab. 1 and $(335 \pm 5)\,\mathrm{DU}$ is used as VCD_{O_3}. The calculated model output (black) is shown for four different SZAs (25° (dotted), 53° (drawn), 70° (dashed) and 80° (dash-dotted)). The model output and the validation measurement are in good agreement if a model SZA of 53° is used, which is equivalent to the SZA during the measurement time. The model uncertainty is shown in shaded grey.

3.3 Results of the field measurements

Volcanic plume measurements were performed on July 22, 2019, 08:50 - 09:10 CET. The instrument was pointing towards the plume of Mt. Etna's South East crater with a constant viewing direction (azimuth 204°N, elevation 5°, see Fig. 5). The wind direction was $\approx 5°\mathrm{N}$ with a velocity of $\approx 6\,\mathrm{m\,s^{-1}}$ (wind data from UWYO). Hence, the plume was partly covered by the crater flank. The frame rate during the measurement was 0.2 Hz for a pair (I_A and I_B) of images.
The flat-field correction was performed as described in section 3.2, using the arithmetic mean over ~~five~~ ten dark images and five flat-field images, obtained in a plume free sky region. An exemplary set of volcanic plume SO_2 images, obtained with the IFPICS instrument in on-band setting I_A and off-band setting I_B, are shown in Fig. 6. Further images of I_A and I_B are shown in Appendix A. The circular shape of the retrieved image arises from the FPI's circular clear aperture limiting the imaging FOV.
The IFPICS SO_2 AA $\tilde{\tau}_{SO_2}$ is calculated pixel-wise according to Eq. 1 from I_A and I_B. For the conversion into SO_2 CD S_{SO_2} the forward instrument model (Eq. 2 - 7) is inverted by least square fitting of a 4th order polynomial to the calculated CD relation $S_{SO_2}(\tilde{\tau}_{SO_2})$. The model input parameters of the instrument are shown in Tab. 1. The SZA during the time of the measurement is $(78 \pm 3)°$ (NOAA) with a VCD_{O_3} of $335 \pm 5\,\mathrm{DU}$ (according to TEMIS database; Veefkind et al., 2006). The

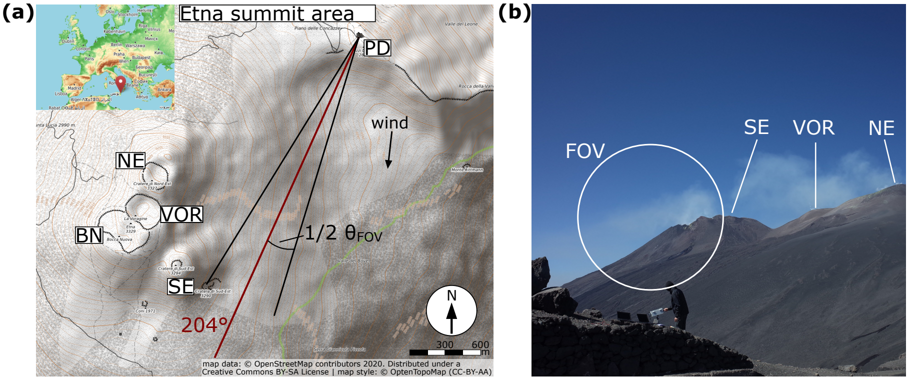

Figure 5. **(a)**: Topographic map of the Mt. Etna summit area, North East crater (NE), Voragine (VOR), Bocca Nuova (BN), South East crater (SE) and measurement location at the Osservatorio Vulcanologico Pizzi Deneri (PD) are indicated. The viewing direction on 22 July 2019 is 204° (red drawn) with an FOV of $\theta_{FOV} = 18°$ (black drawn) and an elevation of 5°. The FOV is partly covering the plume emanating from SE crater. The average wind direction is ≈ 5° with a speed of ~~≈ 6 m/s~~ $\approx 6\,\mathrm{m\,s^{-1}}$ (wind data from UWYO). **(b)**: Visual image of the volcanic plume on 22 July 2019 with indicated camera field of view (FOV).

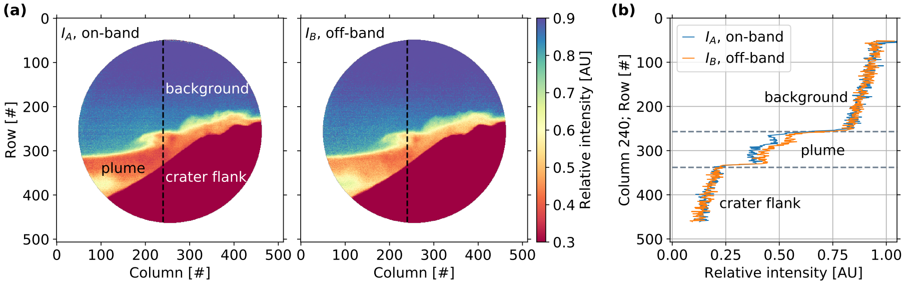

Figure 6. **(a)**: Flat-field corrected intensity images (400×400 pixel) acquired with the IFPICS prototype in on-band I_A and off-band setting I_B. The I_A image shows the expected higher SO_2 absorption in comparison with I_B ($I_A < I_B$ in plume region). The plume is visible in both images due to the broad band SO_2 absorption and other extinction in the measurement spectral range. The circular image shape arise from the FPIs circular clear aperture. **(b)**: Intensity column 240 (dashed black lines in (a)) for I_A (blue) and I_B (orange). The enhanced absorption (reduced intensity) is clearly visible in the plume section with $I_A < I_B$, whereas in the background sky and crater flank sections the intensities are equal $I_A = I_B$.

retrieved calibration function $S_{\mathrm{SO_2}}(\tilde{\tau}_{\mathrm{SO_2}})$ is

$$S_{\mathrm{SO_2}}(\tilde{\tau}_{\mathrm{SO_2}}) = \sum_{0}^{4} x_i \cdot \tilde{\tau}^{i}_{\mathrm{SO_2}} \tag{8}$$

with ~~$x_0 = 1.0 \times 10^{13}$, $x_1 = 1.1 \times 10^{19}$, $x_2 = 9.3 \times 10^{18}$, $x_3 = 7.9 \times 10^{18}$, and $x_4 = 1.6 \times 10^{19}$~~ $x_0 \overset{!}{=} 0$, $x_1 = 1.8 \times 10^{19}$, $x_2 = 1.7 \times 10^{19}$, $x_3 = 1.7 \times 10^{19}$, and $x_4 = 6.6 \times 10^{19}$ in units of $\mathrm{molec\,cm^{-2}}$ respectively with x_0 fixed to zero. This approximation yields an average relative deviation of ~~0.006 %~~ 0.007 % for $S_{\mathrm{SO_2}}$ from the modelled value, with a maximum relative

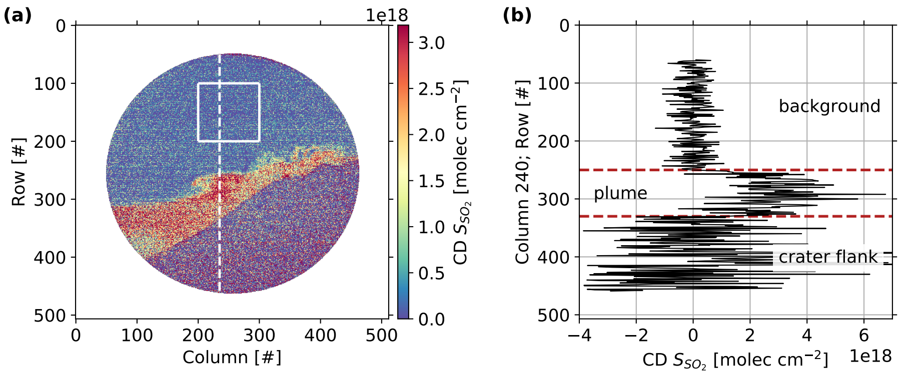

Figure 7. (a): Volcanic plume SO_2 CD distribution calculated from images acquired with the IFPICS prototype and using the instrument forward model conversion function $S_{SO_2}(\tilde{\tau}_{SO_2})$ (see Eq. 8). The plume free area indicated by a white square (100 × 100 pixel) is used to correct for atmospheric background and to obtain an estimation for the detection limit. **(b)**: Individual SO_2 CD column 240 (indicated by dashed white line in (a)) showing that background, plume, and crater flank region are clearly distinguishable. High scattering in the crater flank region is induced by low radiance.

deviation of ~~0.07 %~~ 0.08 % for small SO_2 CDs.

An evaluated image of the volcanic plume SO_2 CD distribution corresponding to the intensities shown in Fig. 6 is shown in Fig. 7. Further evaluated CD distribution images of the same time series are presented in Appendix A. A time series of the plume evolution is visualised in a flip-book from the supplementary material.

The volcanic plume of Mt. Etna's South East crater is clearly visibly and reaches SO_2 CDs higher than $3 \times 10^{18}\,\mathrm{molec\,cm^{-2}}$. The atmospheric background is $S_{SO_2,bg} = 4.3 \times 10^{16}\,\mathrm{molec\,cm^{-2}}$ and was determined by the arithmetic mean over a plume free area within the evaluated image (white square, 100 × 100 pixel, in Fig. 7, (a)). Since the $S_{SO_2,bg}$ is determined from an evaluated CD distribution image it accounts for the residual signal in S_{SO2} between the direction of the volcanic plume and the direction of the flat-field images used in the evaluation. The $S_{SO_2,bg}$ was subtracted from the displayed image in the final step of the evaluation. The similar plume free area (white square, 100 × 100 pixel, in Fig. 7, (a)) is further used to give an estimation for the SO_2 detection limit of the IFPICS prototype by calculating the 1-σ pixel-pixel standard deviation. The obtained detection limit ~~is $5.5 \times 10^{17}\,\mathrm{molec\,cm^{-2}\,s^{-1/2}}$~~ for an exposure time of one second is $5.5 \times 10^{17}\,\mathrm{molec\,cm^{-2}}$ given by the noise equivalent signal. The measurements were performed in the morning with an SZA of 78° and therefore reduced sensitivity and under relatively low light conditions. For decreasing SZA the sensitivity will increase according to Fig. 4 and the increasing sky radiance will reduce the photon shot noise. ~~I.e.~~ In other words, the gas cell measurements (taken at SZA of 53°, with approximately twice the sky radiance compared to SZA of 78°) show a detection limit of ~~$2.1 \times 10^{17}\,\mathrm{molec\,cm^{-2}\,s^{-1/2}}$~~ $2.1 \times 10^{17}\,\mathrm{molec\,cm^{-2}}$ for an exposure time of one second. For ideal measurement conditions (lowest SZA, highest sky radiance) the detection limit will be further improved.

After the proof of concept, showing the capability of IFPICS to determine SO_2 CD images it is possible to determine fluxes from a CD image time series. Especially, if the series allows to trace back individual features in consecutively recorded images it can be used to directly determine the plume velocity using the approach of cross-correlation (e.g. McGonigle et al., 2005; Mori and Burton, or optical flow algorithms (e.g. Kern et al., 2015b) and to determine the plume propagation direction (e.g. Klein et al., 2017) . However, the viewing geometry on the day of our measurement was unfavourable as it was not possible to reach another measurement location due to a lack in infrastructure. The plume propagation direction and central line of sight show an inclination of 19° only, resulting in high pixel contortions, especially for pixel close to the edges of the FOV. Further, significant parts of the plume are covered by the crater flank due to its propagation direction. For the sake of completeness, we would like to give a rough estimate on the SO_2 flux obtained from our data.

The SO_2 flux Φ_{SO_2} is determined by integrating the SO_2 CD along a transect through the volcanic plume and subsequent multiplication by the wind velocity perpendicular to the FOV direction, however due to the viewing geometry issues we will use external wind data (direction: 5°; velocity $v_{wind} \approx 6\,\mathrm{m\,s^{-1}}$ (data from UWYO)) for the calculation. As the camera pixel size is finite the integral is replaced by a discrete summation over the pixel n

$$\Phi_{SO_2} = v_\perp \sum_n S_{SO_2,n} \cdot h_n \tag{9}$$

including the perpendicular wind velocity $v_\perp$, the SO_2 CD $S_{SO_2,n}$ and the pixel extent h_n. The perpendicular wind velocity can directly be calculated from geometric considerations (see Fig. 5,(a)), accounting to $v_\perp \approx \sin(19°) \cdot v_{wind} \approx 2\,\mathrm{m\,s^{-1}}$. To determine the pixel extent the distance between the volcanic plume and the location of measurement is required. In the centre of the FOV this distance is $\approx 3500\,\mathrm{m}$ yielding $h_n \approx 2.7\,\mathrm{m}$. To keep the impact of pixel contortions low the plume transect is located centrally in the FOV at column 250 and ranging from rows $n = 230$ to 330. Using these quantities, we retrieve a mean SO_2 mass flux for the measurement of $\Phi_{SO_2} = (84 \pm 11)\,\mathrm{t\,d^{-1}}$ for the investigated plume of the South East crater, which is comparable to previous flux measurements of the South East crater (Aiuppa et al., 2008; D'Aleo et al., 2016). Nevertheless, the flux should be regarded as lower limit, since the plume was covered by crater flank to an unknown extent.

4 Conclusion

By imaging and quantifying the SO_2 distribution in the volcanic plume of Mt. Etna we successfully demonstrate the feasibility of the IFPICS technique proposed by Kuhn et al. (2014). We were able to unequivocally resolve the dynamical evolution of SO_2 in a volcanic plume with a high spatial and temporal resolution (400×400 pixel, 1 s integration time, 4×4 binning). The retrieved detection limit for the SO_2 measurement is $5.5 \times 10^{17}\,\mathrm{molec\,cm^{-2}\,s^{-1/2}}$. The detection limit however varies with the SZA and can reach values below $2 \times 10^{17}\,\mathrm{molec\,cm^{-2}\,s^{-1/2}}$ under ideal conditions, comparable to traditional SO_2 imaging techniques (see Kern et al., 2015a). Also, the imaging technique lends itself to the determination of gas fluxes and we obtained an SO_2 mass flux of $\Phi_{SO_2} = (84 \pm 11)\,\mathrm{t\,d^{-1}}$ for Mt. Etna's South East crater plume. However, due to unfavourable conditions in the viewing geometry the retrieved flux should be treated as a lower limit. In general, it is possible to apply optical flow algorithms on image series acquired under more ideal viewing geometry conditions (e.g. Kern et al., 2015b). These allow to determine the plume velocity and angle between the observation direction and plume propagation direction in order to retrieve accurate SO_2 fluxes (e.g. Klein et al., 2017).

The specific spectral detection scheme of IFPICS allows to use a numerical instrument model to directly convert the measured AA $\tilde{\tau}$ into CD S distributions. This inherent calibration method makes in-field calibrations methods, e.g. by gas cells, unnecessary. The accuracy of the instrument model could be demonstrated using $\mathrm{SO_2}$ cells with a known CD, determined by simultaneous DOAS measurements.

Our IFPICS instrument is still an early stage prototype. The employed optics are highly modular allowing easy adjustments even outside a laboratory. The physical dimensions of < 10 litres, and $< 5\,\mathrm{kg}$ and the low power consumption of $< 10\,\mathrm{W}$ combined with the fact that no maintenance and in-field calibration is needed, make it already a close to ideal field instrument. Furthermore, the temporal resolution of the instrument can further be increased by replacing the employed sensor as it does not allow for time-optimised control of image acquisition.

Compared to traditional $\mathrm{SO_2}$ cameras the minimised cross interferences to broad band plume extinction increases the selectivity and thus should allow to apply the IFPICS technique to much weaker $\mathrm{SO_2}$ sources. Furthermore, the ~~small~~ expected smaller interference to broadband effects ~~extends~~ in comparison to traditional $\mathrm{SO_2}$ imaging techniques should allow to extend the range of meteorological conditions acceptable for field measurement (see Kuhn et al., 2014). ~~Also, the imaging technique lends itself to the determination of gas fluxes. For instance the wind velocity and also the angle between the observation direction and plume propagation direction can be determined from the images series (see e.g. Klein et al., 2017).~~

The demonstrated IFPICS technique is not limited to the detection of $\mathrm{SO_2}$. In general the technique is applicable to numerous further trace gases which show a distinct pattern (ideally periodic) in their absorption spectrum (see Kuhn et al., 2019). In the case of volcanic emissions detectable trace species are e.g. bromine monoxide BrO or chlorine dioxide OClO. Beyond volcanic applications IFPICS could be used to investigate e.g. air pollution by measuring nitrogen dioxide $\mathrm{NO_2}$ or formaldehyde HCHO.

Appendix A

Further evaluated images of the time series acquired on July 22, 2019, 08:50 - 09:10 CET at Mt. Etna, Italy are shown in Fig. A1. The evaluation procedure is analogous to the routine explained in Section 3.3. The time difference between a set (1 - 4) of images accounts for $\approx 120\,\mathrm{s}$ and allows to trace back plume dynamics.

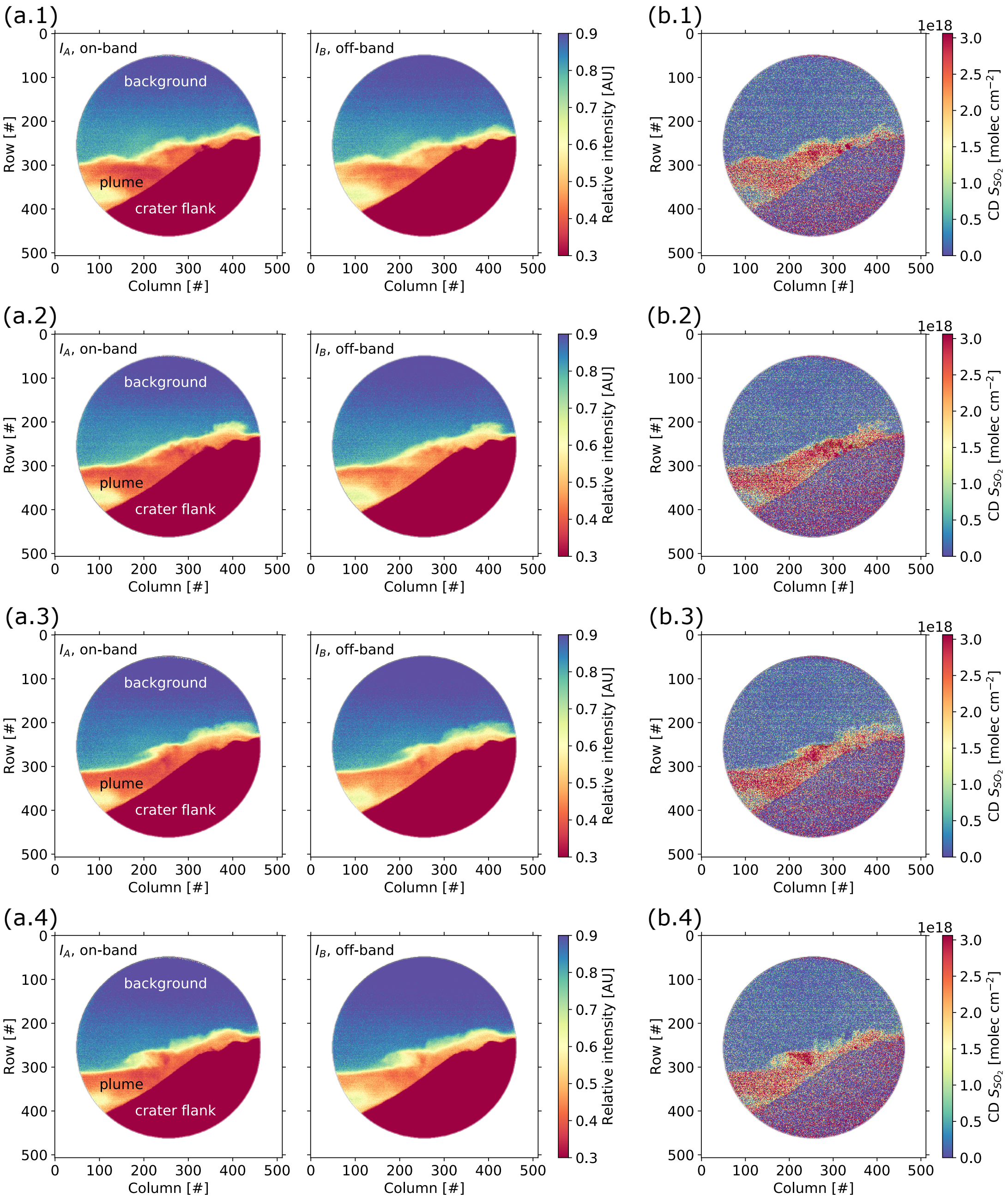

Figure A1. Exemplary set of evaluated images (400×400 pixel) acquired with the IFPICS prototype on 22~~.~~July 2019, 08:50 - 09:10 CET at Mt. Etna, Italy. The time difference between each set of images (**1-4**) accounts for $\approx 120\,\mathrm{s}$, allowing to trace back plume dynamics. **(a)**: Flat-field corrected intensity images I_A and I_B. **(b)**: Volcanic plume SO_2 CD S_{SO_2} distribution calculated with the conversion function shown in Eq. 8.

Data availability. The data can be obtained from the authors upon request.

Author contributions. JK, NB and UP developed the question of research. JK, NB and CF conducted the field campaign. JK and CF developed the instrument model. CF designed, constructed and characterised the instrument, evaluated the data and wrote the manuscript with all authors contributing by revising it within several iterations.

Competing interests. The authors declare that they have no conflict of interest.

Acknowledgements. We would like to thank *SLS Optics Ltd.* for sharing their expertise in designing and manufacturing the etalons. Support by the Deutsche Forschungsgemeinschaft (project DFG PL 193/23-1) is gratefully acknowledged. We also thank Emmanuel Dekemper and Toshiya Mori for their valuable and constructive reviews.

References

Aiuppa, A., Giudice, G., Gurrieri, S., Liuzzo, M., Burton, M., Caltabiano, T., McGonigle, A. J. S., Salerno, G., Shinohara, H., and Valenza, M.: Total volatile flux from Mount Etna, Geophysical Research Letters, 35, https://doi.org/10.1029/2008gl035871, 2008.

Bluth, G., Shannon, J., Watson, I., Prata, A., and Realmuto, V.: Development of an ultra-violet digital camera for volcanic SO2 imaging, Journal of Volcanology and Geothermal Research, 161, 47–56, 2007.

Bogumil, K., Orphal, J., Homann, T., Voigt, S., Spietz, P., Fleischmann, O., Vogel, A., Hartmann, M., Kromminga, H., Bovensmann, H., Frerick, J., and Burrows, J.: Measurements of molecular absorption spectra with the {SCIAMACHY} pre-flight model: instrument characterization and reference data for atmospheric remote-sensing in the 230-2380 nm region, Journal of Photochemistry and Photobiology A: Chemistry, 157, 167 – 184, https://doi.org/http://dx.doi.org/10.1016/S1010-6030(03)00062-5, http://www.sciencedirect.com/science/article/pii/S1010603003000625, atmospheric Photochemistry, 2003.

Chance, K. and Kurucz, R.: An improved high-resolution solar reference spectrum for earth's atmosphere measurements in the ultraviolet, visible, and near infrared, J. Quant. Spec. Rad. Trans., 111, 1289–1295, https://doi.org/10.1016/j.jqsrt.2010.01.036, http://www.sciencedirect.com/science/article/pii/S0022407310000610, 2010.

D'Aleo, R., Bitetto, M., Donne, D. D., Tamburello, G., Battaglia, A., Coltelli, M., Patanè, D., Prestifilippo, M., Sciotto, M., and Aiuppa, A.: Spatially resolved SO2 flux emissions from Mt Etna, Geophysical Research Letters, 43, 7511–7519, https://doi.org/10.1002/2016gl069938, 2016.

Dekemper, E., Vanhamel, J., Van Opstal, B., and Fussen, D.: The AOTF-based NO 2 camera, Atmospheric Measurement Techniques, 9, 6025, 2016.

Kern, C., Lübcke, P., Bobrowski, N., Campion, R., Mori, T., Smekens, J.-F., Stebel, K., Tamburello, G., Burton, M., Platt, U., and Prata, F.: Intercomparison of SO2 camera systems for imaging volcanic gas plumes, Journal of Volcanology and Geothermal Research, 300, 22–36, https://doi.org/10.1016/j.jvolgeores.2014.08.026, 2015a.

Kern, C., Sutton, J., Elias, T., Lee, L., Kamibayashi, K., Antolik, L., and Werner, C.: An automated SO2 camera system for continuous, real-time monitoring of gas emissions from Kīlauea Volcano's summit Overlook Crater, Journal of Volcanology and Geothermal Research, 300, 81–94, https://doi.org/10.1016/j.jvolgeores.2014.12.004, 2015b.

Klein, A., Lübcke, P., Bobrowski, N., Kuhn, J., and Platt, U.: Plume propagation direction determination with SO_2 cameras, Atmospheric Measurement Techniques, 10, 979–987, https://doi.org/10.5194/amt-10-979-2017, 2017.

Kuhn, J., Bobrowski, N., Lübcke, P., Vogel, L., and Platt, U.: A Fabry Perot interferometer-based camera for two-dimensional mapping of SO_2 distributions, Atmospheric Measurement Techniques, 7, 3705–3715, https://doi.org/10.5194/amt-7-3705-2014, http://www.atmos-meas-tech.net/7/3705/2014/, 2014.

Kuhn, J., Platt, U., Bobrowski, N., and Wagner, T.: Towards imaging of atmospheric trace gases using Fabry–Pérot interferometer correlation spectroscopy in the UV and visible spectral range, Atmospheric Measurement Techniques, 12, 735–747, https://doi.org/10.5194/amt-12-735-2019, 2019.

Lübcke, P., Bobrowski, N., Illing, S., Kern, C., Nieves, J. M. A., Vogel, L., Zielcke, J., Granados, H. D., and Platt, U.: On the absolute calibration of SO2 cameras, Atmospheric Measurement Techniques, 6, 677–696, https://doi.org/10.5194/amt-6-677-2013, 2013.

McGonigle, A. J. S., Hilton, D. R., Fischer, T. P., and Oppenheimer, C.: Plume velocity determination for volcanic SO2 flux measurements, Geophysical Research Letters, 32, https://doi.org/10.1029/2005GL022470, https://agupubs.onlinelibrary.wiley.com/doi/abs/10.1029/2005GL022470, 2005.

Mori, T. and Burton, M.: The SO2 camera: A simple, fast and cheap method for ground-based imaging of SO2 in volcanic plumes, Geophysical Research Letters, 33, 2006.

NOAA: NOAA, Global Monitoring Division, Solar Geometry Calculator, accessed 2020-04, https://www.esrl.noaa.gov/gmd/grad/antuv/SolarCalc.jsp.

Perot, A. and Fabry, C.: On the Application of Interference Phenomena to the Solution of Various Problems of Spectroscopy and Metrology, The Astrophysical Journal, 9, 87, https://doi.org/10.1086/140557, 1899.

Platt, U. and Stutz, J.: Differential optical absorption spectroscopy, Springer Verlag, 2008.

Platt, U., Lübcke, P., Kuhn, J., Bobrowski, N., Prata, F., Burton, M., and Kern, C.: Quantitative imaging of volcanic plumes - Results, needs, and future trends, Journal of Volcanology and Geothermal Research, 300, 7–21, https://doi.org/10.1016/j.jvolgeores.2014.10.006, 2015.

Serdyuchenko, A., Gorshelev, V., Weber, M., Chehade, W., and Burrows, J. P.: High spectral resolution ozone absorption cross-sections - Part 2: Temperature dependence, Atmos. Meas. Tech., 7, 625–636, https://doi.org/10.5194/amt-7-625-2014, http://www.atmos-meas-tech.net/7/625/2014/, 2014.

UWYO: University of Wyoming, Department of Atmopsheric Science, atmospheric soundings; Station data: Trapani (LICT), Italy 2019-07-22 12:00; accessed 2020-04, http://weather.uwyo.edu/upperair/sounding.html.

Vargas-Rodríguez, E. and Rutt, H.: Design of CO, CO2 and CH4 gas sensors based on correlation spectroscopy using a Fabry–Perot interferometer, Sensors and Actuators B: Chemical, 137, 410–419, https://doi.org/10.1016/j.snb.2009.01.013, 2009.

Veefkind, J., de Haan, J., Brinksma, E., Kroon, M., and Levelt, P.: Total ozone from the ozone monitoring instrument (OMI) using the DOAS technique, IEEE Transactions on Geoscience and Remote Sensing, 44, 1239–1244, https://doi.org/10.1109/tgrs.2006.871204, 2006.

Veefkind, J., Aben, I., McMullan, K., Förster, H., de Vries, J., Otter, G., Claas, J., Eskes, H., de Haan, J., Kleipool, Q., van Weele, M., Hasekamp, O., Hoogeveen, R., Landgraf, J., Snel, R., Tol, P., Ingmann, P., Voors, R., Kruizinga, B., Vink, R., Visser, H., and Levelt, P.: TROPOMI on the ESA Sentinel-5 Precursor: A GMES mission for global observations of the atmospheric composition for climate, air quality and ozone layer applications, Remote Sensing of Environment, 120, 70–83, https://doi.org/10.1016/j.rse.2011.09.027, 2012.

Wilson, E. L., Georgieva, E. M., and Heaps, W. S.: Development of a Fabry–Perot interferometer for ultra-precise measurements of column CO2, Measurement Science and Technology, 18, 1495–1502, https://doi.org/10.1088/0957-0233/18/5/040, 2007.